1-1-2015

Hierarchically porous carbon-zirconium carbide spheres as potentially reusable transmutation targets

Nicholas Scales
University of Wollongong, ns112@uowmail.edu.au

Jun Chen
University of Wollongong, junc@uow.edu.au

Tracey L. Hanley
ANSTO

Daniel P. Riley
ANSTO

Gregory R. Lumpkin
ANSTO

See next page for additional authors

Hierarchically porous carbon-zirconium carbide spheres as potentially reusable transmutation targets

Abstract

The preparation of hierarchically porous phase-pure carbon-zirconium carbide spheres with surface areas upwards of 70 m^2/g and diameters in the 1-2 mm range has been achieved. The zirconium carbide beads were prepared through carbothermal reduction of polyacrylonitrile-zirconium composites prepared via three different routes including infiltration of a zirconium precursor into preformed polyacrylonitrile (PAN) beads and two one-pot co-precipitation methods. Depending on the route used to prepare the composites, relatively high surface area phase-pure zirconium carbides with the radial macroporous internal structure of the PAN template could be prepared. The adsorption of the elements U, Mo, Cs and Sr by the zirconium carbide beads was studied as a function of pH in the range 1-13 and target element concentrations of 0.025 mmol/L. The as-prepared hierarchical zirconium carbide beads demonstrated almost quantitative uptake of Mo below pH 4 with uptake decreasing to close to zero and above pH 10.5. On the other hand, U uptake was negligible below pH 4 and became quantitative in the range 4-12. Cesium was not extracted to any significant extent in the pH range studied and Sr only to a limited extent above pH 10. The engineered hierarchical porosities, neutron transparency, thermal stability and anticipated chemical stability of the present zirconium carbide spheres makes them promising candidates as reusable transmutation targets for Minor Actinide incineration.

Keywords

reusable, transmutation, targets, hierarchically, carbon, porous, zirconium, carbide, spheres, potentially

Disciplines

Engineering | Physical Sciences and Mathematics

Publication Details

Scales, N., Chen, J., Hanley, T. L., Riley, D. P., Lumpkin, G. R. & Luca, V. (2015). Hierarchically porous carbon-zirconium carbide spheres as potentially reusable transmutation targets. Microporous and Mesoporous Materials, 212 100-109.

Authors

Nicholas Scales, Jun Chen, Tracey L. Hanley, Daniel P. Riley, Gregory R. Lumpkin, and Vittorio Luca

Hierarchically porous carbon–zirconium carbide spheres as potentially reusable transmutation targets

Nicholas Scales [a], Jun Chen [b], Tracey L. Hanley [a], Daniel P. Riley [a], Gregory R. Lumpkin [a], Vittorio Luca [c, *]

[a] Institute of Materials Engineering, Australian Nuclear Science and Technology Organisation, Locked Bag 2001, Kirrawee DC, New South Wales 2232, Australia
[b] Intelligent Polymer Research Institute, ARC Centre of Excellence for Electromaterials Science, Australian Institute of Innovative Materials, University of Wollongong, Innovation Campus, North Wollongong, New South Wales 2522, Australia
[c] Comision Nacional de Energía Atomica, Centro Atomico Constituyentes, Av. General, Paz 1499, 1650 San Martin, Provincia de Buenos Aires, Argentina

a r t i c l e i n f o

Article history:
Received 4 December 2014
Received in revised form
19 March 2015
Accepted 20 March 2015
Available online 28 March 2015

Keywords:
Hierarchical porosity
Zirconium carbide
Polyacrylonitrile
Transmutation
Minor Actinides

a b s t r a c t

The preparation of hierarchically porous phase-pure carbon–zirconium carbide spheres with surface areas upwards of 70 m^2/g and diameters in the 1–2 mm range has been achieved. The zirconium carbide beads were prepared through carbothermal reduction of polyacrylonitrile-zirconium composites pre- pared via three different routes including infiltration of a zirconium precursor into preformed poly-acrylonitrile (PAN) beads and two one-pot co-precipitation methods. Depending on the route used to prepare the composites, relatively high surface area phase-pure zirconium carbides with the radial macroporous internal structure of the PAN template could be prepared. The adsorption of the elements U, Mo, Cs and Sr by the zirconium carbide beads was studied as a function of pH in the range 1–13 and target element concentrations of 0.025 mmol/L. The as-prepared hierarchical zirconium carbide beads demonstrated almost quantitative uptake of Mo below pH 4 with uptake decreasing to close to zero and above pH 10.5. On the other hand, U uptake was negligible below pH 4 and became quantitative in the range 4–12. Cesium was not extracted to any significant extent in the pH range studied and Sr only to a limited extent above pH 10. The engineered hierarchical porosities, neutron transparency, thermal stability and anticipated chemical stability of the present zirconium carbide spheres makes them promising candidates as reusable transmutation targets for Minor Actinide incineration.

1. Introduction

Non-oxide ceramics such as zirconium carbide (ZrC) and silicon carbide (SiC) are high refractory ceramics with good thermo-mechanical properties. Of the two, ZrC is particularly advantageous for certain applications as it has a higher melting point (3400 °C), hardness, fracture toughness and strength. It is also a good thermal and electrical conductor. These properties make ZrC especially desirable in many nuclear applications. ZrC has been studied as a potential material for ceramic coated fuels and has shown excellent resistance to neutron irradiation performing better than SiC [1–4].

Due to the low neutron cross-section of both of these carbides as well as their inherent stability they can also be considered as transmutation hosts. Transmutation refers to the ability to transform one type of atom into another by changing its nuclear structure. This can be accomplished by bombarding the atoms of interest with neutrons either in a nuclear reactor or in an accelerator driven fission-system. In the context of irradiated nuclear fuel, transmutation can for instance, convert Pu and other radiotoxic and long-lived radionuclides into radionuclides with more favourable characteristics, *viz* shorter half-lives [5]. A large international research effort has been underway for many years with the objective of separating highly radiotoxic nuclides into separate fractions, recycling those with high energy value, and dealing with the others independently [6,7]. Among these radionuclides, the Minor Actinides (MAs) Np, Am and Cm are the most significant contributors to the long-term radiotoxicity of spent fuel. If these

* Corresponding author.
E-mail address: vluca@cnea.gov.ar (V. Luca).

elements are extracted, the time taken for the radiotoxicity of spent fuel to return to the same level as the starting U ore, could be reduced from hundreds of thousands of years, to mere hundreds of years.

The variety of parameters to be considered in MA incineration and design of targets and fuels, including core physics, chemical stability, radiation tolerance and thermal conductivity, have already been reviewed in great detail [5]. So far, a promising assortment of candidate materials for use as targets and fuels (including the so-called Inert Matrix Fuels (IMFs)) in the incineration of MAs, have been described and their performances under different irradiation conditions elucidated. These include actinide metal-containing alloys and composites, oxides, nitrides, carbides, MgO, $MgAl_2O_4$ (spinel), yttrium-stabilised ZrO_2 (YSZ) and $Y_3Al_2O_5$ (yttrium aluminium garnet or YAG) [8e18]. This list is by no means exhaustive. Generally these materials incorporate MAs into the host matrix either as part of a solid-solution or interdispersed as a separate phase. One drawback of most of these refractory ceramic compacts and monoliths is that they are fully dense and therefore cannot be readily recycled. This technology might be improved by development of a reusable target or IMF with accessible porosity onto whose interior surface target radionuclides could be deposited prior to neutron irradiation. Deposition could be achieved by infiltration and/or precipitation, or better still, adsorption pro- cesses. Notably, an infiltration approach has already been applied to the synthesis of (presumably non-recyclable) actinide-loaded fuel kernels from non-radioactive and porous $MgAl_2O_4$ [19] and YSZ spheres pre-formed by sol**e**gel method [20,21]. Stripping of the less long-lived fission products post-irradiation from this proposed porous composite matrix would in theory permit recycling of the porous target, greatly minimising total waste volumes and there- fore reducing costs associated with long-term storage. Moreover, it stands to reason that a porous target may also mitigate the effects of He generation (bubble/void formation and swelling) and thereby outperform its fully dense counterpart with respect to physical stability. The general features of such a support material would ideally include 1) high chemical and radiation stability, 2) ease of incorporation of MAs, 3) high neutron transparency and 4) good thermal conductivity.

However, for such a material to be viable for the said purpose, it would need to be easily prepared and would have to possess suitable morphology, porosity and adsorption properties such that loading with MAs could be achieved by some convenient means. Since ZrC has excellent thermomechanical and thermoelectrical properties and is under consideration as an IMF for the transmutation of MAs [22], we would consider hierarchically porous ZrC spheres to be ideal for this purpose.

Traditionally, preparation of ZrC involves carbothermal reduction of a zirconium precursor (Zr or ZrO_2) using graphite as the reductant at temperatures above 1800 °C. However recently, sol-**e**gel and other methods that produce molecular-scale mixing of the precursors have shown that ZrC can be prepared at much lower temperatures, sometimes as low as 900 ° C [23]. The tangible benefit of these latter methods is that fabrication of ZrC-based materials can be achieved with common laboratory equipment making synthesis of ZrC-based spheres highly feasible.

The aim of the present work is the synthesis and characterisation of porous ZrC spheres for potential application as reusable transmutation targets or IMFs for the incineration of MAs or other long-lived by-products of conventional nuclear power generation. To this end, we have used three different methods to produce composites beads of polyacrylonitrile (PAN) and Zr precursors and have subjected the resulting monolithic materials to carbothermal reduction at the lowest temperatures possible in order to form the desired ZrC phase. PAN beads formed through a gelation process, are a promising template structure as they typically possess an hierarchical and radial pore structure well-suited to dynamic or flow-through applications, potentially providing a convenient means to loading with MAs and desorption of their fission products.

2. Experimental

2.1. Chemicals

All chemicals were used as received without further purification. Anhydrous dimethyl sulfoxide (DMSO) (99.9%), zirconium (IV) propoxide (70 wt% solution in 1-propanol), Pluronic F-127, anhydrous ethanol (>99.5%), $ZrCl_4$ (>99.5%), $Na_2MoO_4.2H_2O$ (>99.5%), $CsNO_3$ (99.999%) and $Sr(NO_3)_2$ (99.995%) were obtained from Sigma Aldrich. $UO_2(NO_3)_2.6H_2O$ (>99%, metals basis) was obtained in house and its purity determined by ICP-MS. Technical grade polyacrylonitrile (PAN) powder was sourced from Yongyi Chemicals, Jiangsu, China. Analytical grade 25 wt% aqueous ammonia, analytical grade 50 wt% aqueous sodium hydroxide and trace metal analytical grade 69% nitric acid were sourced from Merck, Australia. The 3.5 mol% H_2 in Ar gas mix was sourced from Coregas, Australia. Milli-Q® high purity water (18.2 MU cm) was sourced via a Millipore system.

2.2. Nomenclature

Synthesised materials were designated as ZrAC-x, ZrHC-x and ZrAI-x representing materials prepared by alkoxide co-precipitation, halide co-precipitation and alkoxide infiltration, respectively. The value of x represents the Zr content with a value of 1 being the lowest Zr/C ratio and 4 being the highest. For example the first member of the alkoxide infiltrated PAN series is ZrAI-1. PAN bead samples (no Zr content) stabilised at 240 °C and heated to 1350 °C were designated as PAN-240 and PAN-1350, respectively.

2.3. Synthesis

2.3.1. 4 wt% PAN/DMSO precursor solution

A 4 wt% solution of PAN in DMSO was prepared by stirring a mixture of PAN powder and anhydrous DMSO at 50**e**60 °C in a water bath for up to 24 h under nitrogen on a Schlenk line. Aside from keeping the solution under a flow of nitrogen during dissolution and subsampling, no other steps were taken to exclude air and moisture. The result was a viscous golden solution.

2.3.2. Alkoxide co-precipitation route

To warm 4 wt% PAN/DMSO precursor solutions, zirconium (IV) propoxide and Pluronic F-127 were added in the open air. Dissolution was achieved with stirring under a flow of nitrogen. The mass ratios of DMSO/PAN to zirconium (IV) propoxide to Pluronic F-127 were 1:0.11:0.011; 1:0.32:0.011; 1:0.53:0.011 and 1:0.74:0.011.

Using an in-house droplet generator the Zr-containing precur- sor solution was added dropwise to a stirred bath (4 L of deionised water plus 0.5 mL of aqueous 10 wt% F-127 solution), resulting in coagulation of PAN beads. The beads were thoroughly washed to remove surfactant and DMSO then dried to constant weight at low temperature (<35 °C).

2.3.3. Halide co-precipitation route

A fresh subsample of anhydrous $ZrCl_4$ was taken from a nitrogen glove box and then handled thereafter in the open air. To each of 0.75, 1.25, 1.75 and 2.25 g of $ZrCl_4$ respectively, 20 mL of freshly prepared 4 wt% PAN solution in DMSO was added. It proved necessary to add the solution quickly to quench heat evolved by the exothermic reaction between the components, otherwise

decomposition resulted as evident from discolouration of the $ZrCl_4$. The $ZrCl_4$ was dissolved by heating in a water bath at 70 °C with magnetic stirring in a sealed laboratory bottle. The final temperature reached was approximately 65 °C. An aqueous gelation bath at pH 11.1 was prepared by dissolution of 90 g of 25 wt% aqueous ammonia solution in deionised water to produce a total weight of 4 kg. To this aqueous ammonia bath, the $ZrCl_4$/PAN/DMSO precursor solution was added dropwise using a glass syringe and 21 gauge needle, with stirring provided by a paddle stirrer. After the precursor solution was consumed, the bath was stirred for a further 5 min, upon which the beads were collected and thoroughly washed with deionised water to remove DMSO and ammonia. Smooth, shiny and firm beads resulted. The beads were dried to constant weight at low temperature (<35 ° C).

2.3.4. *Alkoxide infiltration route*

To a fresh solution of 4 wt% PAN in DMSO, Pluronic F-127 was added (in weight proportion of 0.95 DMSO/PAN solution to 0.05 Pluronic F-127) and dissolved with stirring. This solution was added dropwise to a stirred bath (4 L of deionised water plus 0.5 mL of 10 wt% Pluronic F-127 solution), using the abovementioned droplet generator and this resulted in coagulation of PAN beads. The beads were thoroughly washed with deionised water to remove surfactant and DMSO then dried to constant weight at low temperature (<35 °C).

Pre-dried PAN beads were further dried in an Heraeus vacuum oven (Thermo Electron, Germany) at 60 °C for five days. Infiltration of the beads was accomplished under air and moisture free conditions on a Schlenk line. Following several minutes of preliminary purging with nitrogen, the beads were pre-evacuated in a Schlenk flask for one hour. Ethanolic solutions of 5, 10, 25 and 50 wt% zirconium (IV) propoxide (70 wt% solution) were prepared in a nitrogen glovebox by gentle stirring. The solutions were sonically degassed for 30 min then transferred to the sealed flask containing the beads while maintaining a dynamic vacuum. After completely submersing the beads in precursor solution, evacuation was continued for a further 15 min, then the flask backfilled with nitrogen, upon which the beads typically sank. The sealed flask was sonicated for 10 min and the beads were collected under suction under ambient air conditions then allowed to air dry by the same method for two hours. Completion of the hydrolysis reaction over three days was achieved in an incubated chamber at 40 °C and 50% relative humidity.

2.4. *Thermal treatment*

2.4.1. *Stabilisation*

The PAN phase of as-produced bead materials was oxidatively stabilised [24] by heat treatment in air at 240 °C for five hours, employing a Thermolyne Type 46200 high temperature furnace with K-type thermocouple. Heating and cooling rates of 1 °C/min were used. The beads were contained in a shallow alumina dish and an alumina shroud was employed to shield bead materials from direct radiant heat.

2.4.2. *High temperature treatment*

Carbothermal reduction was accomplished in an alumina tube furnace (Ceramic Engineering Furnace Manufacturer, Sydney, Australia) at 1350 ° C for 24 h under a reducing atmosphere of 3.5% H_2 in Ar. Heating and cooling rates of 1 ° C/min were used. A graphite foil lined graphite boat with graphite lid (Fig. 1A) (see Supplementary Data) supported on alumina rods, provided a carburising environment for the beads. A 5 mm internal diameter hole in the lid allowed for escape of gaseous by-products. Accurate sample temperature was assured using an alumina sheathed B-type thermocouple (Pyrosales, Sydney, Australia) installed through the centre of the rear tube end cap and positioned near the graphite boat. Gas was supplied to the tube at an outlet pressure of 250 kPa and flow rate of 150 mL/min. Pressure of the exiting gas was regulated with a water bubbler. The alumina tube was pre-purged with reducing gas for 30 min at 1 L/min, equivalent to approximately 11 tube volumes.

2.5. *Characterisation*

2.5.1. *C, H, N microanalysis*

Materials were dried in an Heraeus vacuum oven (Thermo Electron, Germany) in glass vials at 140 °C for 19 h, backfilled with nitrogen, tightly capped and sealed with plastic film to maintain dryness until immediately before analysis. Analysis in duplicate was conducted using a Carlo Erba 1106 instrument. PAN content in the bead materials was estimated from the measured N content, assuming an empirical formula of $(C_3H_3N)_x$ for the PAN homopolymer. Molar ratios of C to N were calculated for each duplicate then averaged.

2.5.2. *Porosimetry and surface area measurements*

Nitrogen gas adsorption was conducted on an ASAP 2020 instrument (Micromeritics, USA) at 77 K (−196 °C). Degassing of samples (typically overnight) was conducted under vacuum at 120 °C for materials heated to 240 ° C, and at 150 ° C for materials heated to 1350 °C. Surface areas were calculated using the BrunauereEmmetteTeller (BET) equation, while the pore volume distributions was determined using BarretteJoynereHallenda (BJH) and Non-Local Density Functional Theory (NLDFT) methods as implemented on the Micromeritics ASAP 2020 software version 3.04. A slit shaped pore model was used to model the experimental data. Such a model is commonly used to model carbon-based materials. The slit pore model gave clearly superior fits to the cylindrical pore model.

2.5.3. *Thermogravimetric analysis (TGA)*

Thermogravimetric analysis was conducted using a TGA Q500 TA instruments mass analyser under air with a heating rate of 10 °C/min from room temperature up to 1000 °C.

2.5.4. *Optical microscopy*

Ground and polished cross-sectional specimens of bead materials were prepared for optical microscopy as follows. Masking tape was used to back PTFE cylindrical molds and the whole beads were affixed to the adhesive tape surface within the mold. The beads were submerged in a two-part epoxy resin (Buehler, USA) and then evacuated for 20 min to remove air. Curing overnight at 35 °C was sufficient to harden the resin. Manual grinding of the resin was conducted with P320 course grit SiC paper, followed by finer grit P800 paper, using a Struers mechanical grinding unit. Polishing was conducted with 1 μm diamond polish and 0.25 μm cloth on a Struers RotoSystem. A Zeiss Axioplan optical microscope was used to collect images of the polished and ground specimens. Images of whole beads were collected using a Wild M400 optical macroscope without any further sample preparation.

2.5.5. *Scanning electron microscopy (SEM)*

Some of the ground and polished specimens used for optical microscopy were reused for examination by SEM. Prior to SEM analysis, all samples were affixed to SEM stubs with double-sided conductive carbon tape and coated with 2e3 nm of Pt. Backscattered electron images were acquired of ground and polished samples using an accelerating voltage of 15 keV, while for fractured surfaces secondary electron images were obtained with an

accelerating voltage of 5 keV. All images were obtained on a Zeiss Ultra Plus instrument.

2.5.6. X-Ray diffraction (XRD)

Powder XRD patterns were acquired with a PANalytical X'pert Pro XRD using Cu weighted K-alpha radiation 1.5406/1.5444 Å 2:1, a step size of 0.0170 °2θ and an effective scan step time of 601.1612 s. Samples were backed with inserts made of single crystal silicon cut off-axis.

Rietveld refinements were undertaken using the Panalytical Highscore Plus 3.0 package, a Rietveld implementation that is based on the source code of the program LHPM from Hill and Howard. A consistent approach was applied to all the Rietveld fits. A pseudo Voigt lineshape function was used and the background was fit with a shifted Chebyshev II polynomial. Isotropic thermal parameters were used in all cases in order not to over determine the data. Given the multiphase nature of most of the patterns, and the problems associated with precisely determining the background, no goodness-of-fit parameters are given. While unit cell dimensions of the major phases in all of the patterns are considered to be well determined, the value for the wt. % of each phase should be considered reasonable estimates rather than accurate determinations.

2.5.7. FT-IR

A Nicolet Nexus 8700 (Thermo Electron Corporation, Madison, WI) instrument fitted with a Smart iTR™ (Attenuated Total Reflectance) accessory was used to collect FT-IR spectra. Each spectrum was an average of 16 scans and acquired with a resolution of 4 cm^{-1}.

2.6. Adsorption studies

2.6.1. pH dependence

For pH dependence studies, 0.025 mmol/L single element solutions were prepared as follows. A 0.025 mmol/L Mo stock was prepared from $Na_2MoO_4.2H_2O$ by dissolution in Milli-Q® water in order to form initially the MoO_4^{2-} species; subsequent pH adjustment with stirring was carried out using either addition of aqueous HNO_3 or NaOH solutions in order to produce Mo solutions with various pH values. 0.025 mol/L single element Cs, Sr and U intermediate stocks were prepared from $CsNO_3$, $Sr(NO_3)_2$ and $UO_2(NO_3)_2.6H_2O$, respectively, dissolved in aqueous 0.01 mol/L HNO_3. This 0.01 mol/L HNO_3 matrix (approximately pH 2) was chosen to stabilise the metal salts in solution and prevent hydrolysis prior to any further dilution. The intermediate stocks were diluted one thousand fold into aqueous HNO_3 or NaOH solutions of various pH values with magnetic stirring. All 0.025 mmol/L stocks were aged for one day, prior to accurate final pH measurement and use in experiments.

Contact experiments for selectivity studies were conducted in batch mode with a volume-to-mass ratio (V/m) of 200 mL/g and a contact time of one day. Gentle agitation was provided with a platform shaker (IKA, Germany) at a shaking rate of approximately 225 rpm. All materials were contacted in triplicate. All 0.025 mmol/L stocks were also carried through this process in triplicate. Solutions after contact were filtered through hydrophilic 0.2 μm syringe filters (Sartorius) and analysed for Mo, Cs, Sr and U on an 820-MS ICP Mass Spectrometer (Bruker, Mulgrave, Australia). Calculated values of % extraction were averaged for each set of triplicates. Errors were estimated from two standard deviations of the triplicates. Some stocks showed measurable precipitation of particular elements under certain conditions, especially U near neutral pH values; these data were excluded.

2.6.2. Recyclability

To test the recyclability for Mo adsorption-desorption, the ZrHC-1 material was contacted with a solution containing 0.025 mmol/L of Mo at V/m of 200 mL/g that had been pH adjusted to 3 using HNO_3. After gentle agitation over a 24 h period a small aliquot of the supernatant was removed and filtered. The sorbed Mo was then desorbed by contacting the solid at the same V/m ratio for similar period using a solution of NaOH at pH of 11. This procedure was repeated thrice more. All filtrates were then analysed by ICP-MS.

3. Results and discussion

3.1. C, N microanalysis

The calculated molar ratios of C to N for the collection of materials (Supplementary data section, Table 1A) ranged from 3.31 to 3.55, which is significantly above the theoretical value of 3.00 based on the PAN homopolymer. The measured ratio for PAN source material was 3.23. These facts taken together suggest that the PAN source material was not the pure homopolymer and also, that considerable residual organic material (such as DMSO) remained in some of the bead structures. Nevertheless, estimates of PAN content in the various bead materials (based on analysis of N content) are given in Table 1. Each series showed the expected decrease in PAN content as Zr precursor was increased.

3.2. Optical microscopy and XRD

Universally, the appearance of the as-produced beads was of cream-coloured spheroids which darkened and exhibited conspicuous shrinkage upon PAN stabilisation at 240 °C and further heat treatment at 1350 °C. Examples of both ZrHC-1 and ZrAI-2 materials at these three stages are given in Fig. 2A, Supplementary Data. The full set of optical microscope images of polished samples for ZrAC-x is supplied in Fig. 3A (see Supplementary Data). In the optical image of ZrAC-1 (Fig. 1e) which is representative of this series, discrete particles presumed to be zirconia could be distinguished. These increased in size as the Zr content was increased.

The XRD patterns of these ZrAC-x materials (Fig. 1a-d) showed the dominant phase to be zirconium carbide for the ZrAC-1 sample although the sample clearly also contained small quantities of impurity phases that could be identified as monoclinic ZrO_2 ($mZrO_2$). As the Zr content was increased, the intensity of reflections due to these $mZrO_2$ phases increased. Rietveld analysis using a two-phase model (ZrC and $mZrO_2$) returned excellent fits and permitted quantification of lattice parameters and phase concentrations (Table 2A) (see Supplementary Data). These data

Table 1
Estimated PAN content in the various bead materials.

Sample	PAN content (wt%)
ZrAC-1	46
ZrAC-2	24
ZrAC-3	16
ZrAC-4	10
ZrHC-1	59
ZrHC-2	51
ZrHC-3	45
ZrHC-4	41
ZrAI-1	74
ZrAI-2	61
ZrAI-3	43
ZrAI-4	24

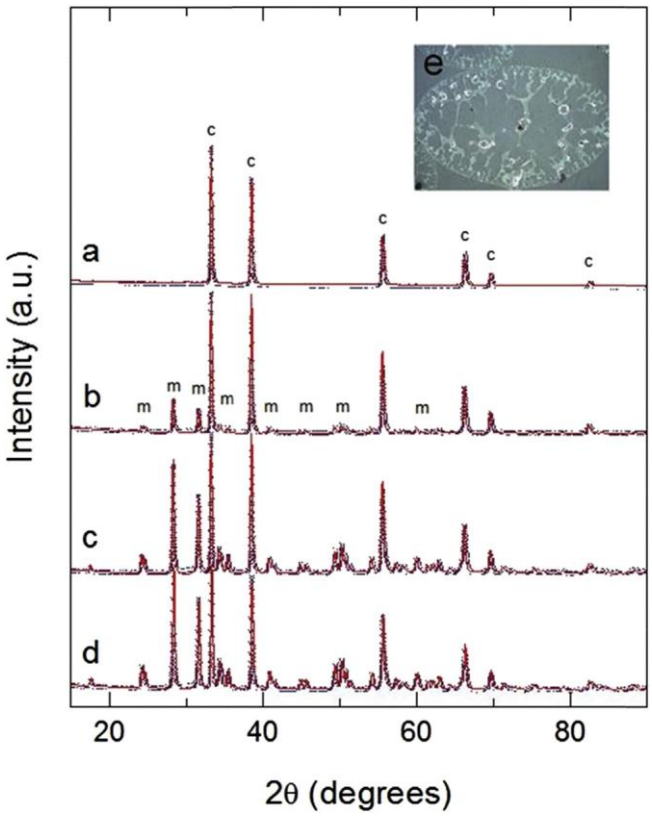

Fig. 1. a**e**d: powder XRD patterns of 1350 °C heat treated alkoxide co-precipitation materials, ZrAC-1 to -4 and Rietveld fits. Key: c, cubic ZrC; m, monoclinic ZrO_2. e: optical microscopy image of 240 °C stabilised ZrAC-1 (full width of image is 1.7 mm).

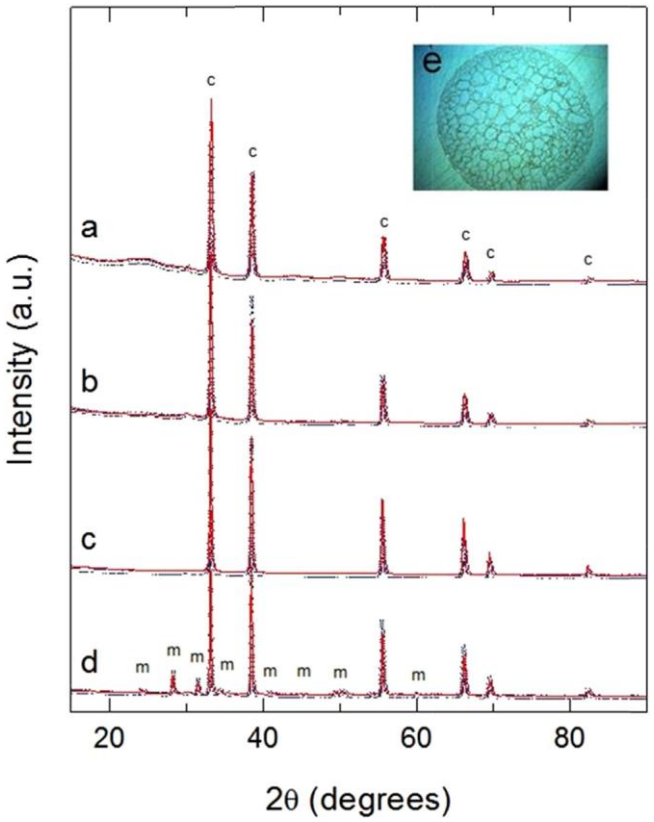

Fig. 2. a**e**d: powder XRD patterns of 1350 °C heat treated alkoxide infiltration materials, ZrAI-1 to -4 and Rietveld fits. Key: c, cubic ZrC; m, monoclinic ZrO_2. e: optical microscopy image of 240 °C stabilised ZrAI-1 (full width of image is 1.7 mm).

confirm that as the proportion of Zr in the reactant precursor solution increased so too did the amount of mZrO_2 that formed as a separate phase. For the ZrAC-4 sample crystalline mZrO_2 was actually the dominant phase. The lattice parameter of the minor ZrC phase was 4.6806 Å corresponding to a C/Zr of about 0.5 according the relationship between unit cell dimension and C/Zr compiled in the review paper by Katoh et al. [25]. That is, the ZrC_x that is being formed under the conditions of preparation relevant to this study is sub-stoichiometric in carbon. The unit cell parameter remained at close to this value as the Zr content of the precursor increased and the mZrO_2 phase crystallized.

As in the case of the ZrAC-x samples, the XRD patterns of the ZrAI-x samples (Fig. 2a**e**d) appear also to be largely mixed phases except in the case of the ZrAI-3 composition that was close to phase pure. The XRD pattern of the ZrAI-1 and ZrAI-2 samples shows crystalline ZrC with lattice parameter very close to that of the ZrAC-x samples. Extremely broad but very weak reflections observed at 25.0, 30.1, 43.83 and 50.0°2q in the patterns of both of these compositions are consistent with the presence of poorly crystalline cubic and tetragonal ZrO_2. Rietveld analysis of the ZrAI-1 was attempted to take these baseline features into account and confirmed the presence of monoclinic and tetragonal or cubic ZrO_2. While these features appear weak, being poorly crystalline and having broad reflections, means that their concentrations could be easily underestimated. In fact, the Rietveld of the ZrAI-1 sample suggests that ZrC accounts for only about 10% of the sample, the rest being comprised mainly of the monoclinic phase (89%) and tetragonal phase (1%). ZrO_2 can also be observed in the optical images of the polished specimens of these compositions as material having bright contrast (Fig. 4A, Supplementary Data). The optical image of ZrAI-1, a representative example, is given in Fig. 3e.

Aside from providing evidence of ZrO_2 crystallization the optical images of both ZrAC-x and ZrAI-x series of materials are similar in having a cellular appearance (viewed in two dimensions) that were evidently macropores, indicating that for the most part the infiltration of beads with epoxy resin was complete.

The Rietveld refinement results for the most phase-pure ZrHC-x samples are summarized in Table 2. Regardless of the method of precursor bead preparation employed, the ZrC phase always has very similar unit cell parameters indicating that the C/Zr ratio remains constant for all samples. In other words the C/Zr ratio depends on the thermal process used rather than the precursor chemistry.

The halide co-precipitation system (ZrHC-x) was visibly different from the other two systems in several respects. First, optical microscope observations of polished specimens of the materials (Fig. 5A, Supplementary Data; a representative sample, ZrHC-1 is also depicted in Fig. 3e) generally showed them to be compositionally homogenous. Second, although the cellular 2D macropore cross-sections were observed, there were also fine porous "islands" near the centre of the beads from the two most Zr rich compositions, seen in many, but not all the beads. Third, there were many air bubbles particularly associated with the centre islands that ostensibly could not be displaced with the epoxy resin. The difficulty in removal of air bubbles during resin infiltration may reflect a lack of pore connectivity. Unlike the interconnected radial pore systems seen in most PAN-based granular materials, the egress of air from the centre island may be restricted with only a few narrow exit points. The centre island was not consistently observed, which could be because the island is only tenuously connected with the outside shell. Consequently, during sample

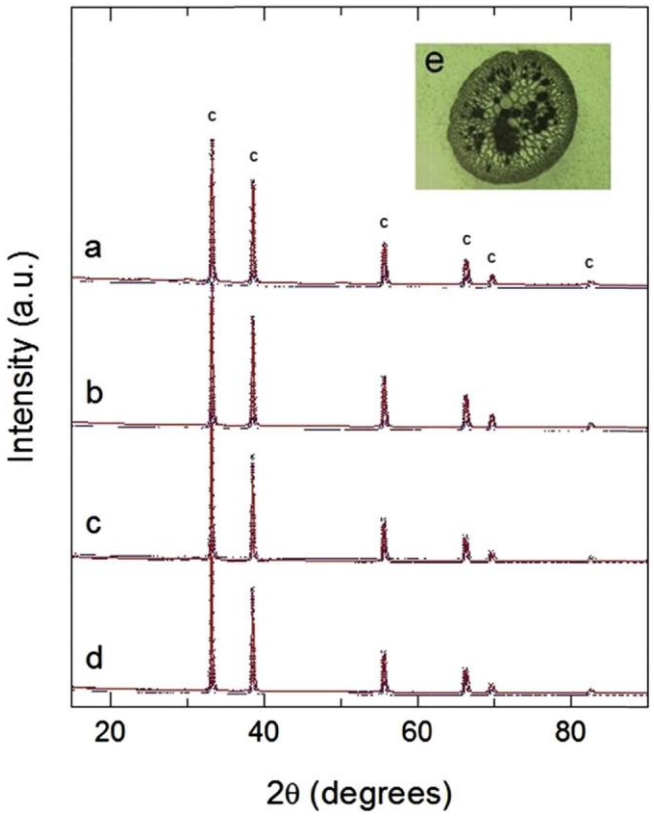

Fig. 3. a**e**d: powder XRD patterns of 1350 ° C heat treated halide co-precipitation materials, ZrHC-1 to -4 and Rietveld fits. Key: c, cubic ZrC. e: optical microscopy image of 240 ° C stabilised ZrHC-1 (full width of image is 2.7 mm).

preparation, the island may sometimes be removed by the grinding and/or polishing processes.

Although cursory inspection of the XRD patterns of the ZrHC-x samples (Fig. 3a**e**d) suggested them to be relatively phase-pure ZrC, closer inspection of the baseline region of the XRD patterns showed the presence of both the monoclinic and tetragonal ZrO_2 phase, albeit as shown by Rietveld analysis at concentrations typically between 1 and 6%. As the Zr content increased the concentration of these impurity phases seemed to decrease. In summary, close inspection of the XRD patterns of all samples clearly indicate the presence of ZrO_2 impurity phases to varying degrees.

3.3. *Scanning electron microscopy (SEM)*

The SEM image of a whole fractured bead (Fig. 4a) demonstrates the radial macropore structure for the three systems. Examination of selected polished samples (Fig. 4b**e**d) revealed detail at smaller length scales than possible with optical microscopy. In the alkoxide co-precipitation material, tiny sub-micron particles of ZrO_2 were dispersed throughout the PAN structure, comprising a continuum of sizes. In the alkoxide infiltration material, the two separate phases of PAN and ZrO_2 could be clearly observed. In the halide co-precipitation material, few distinct domains of ZrO_2 could be seen or distinguished and for the most part the composites appeared homogenous confirming the conclusions from the XRD that this series of materials was close to single phase ZrC with C/Zr close to 0.5.

Diffusion has been identified as a key factor affecting the extent of ZrC formation via carbothermal reduction of ZrO_2 [25]. The success of the present methods can be attributed to efficient mixing of ZrO_2 and PAN (the carbon source) as is evident from SEM, leading to improved reaction kinetics. Moreover, the specific reaction conditions, i.e. use of a reducing atmosphere and graphite boat with lid (giving a carburising or reactive carbon environment), led to a greatly improved result, ostensibly by facilitating irreversible removal of oxygen from the samples as H_2O, CO_2 or CO. Efficacy of the carburising conditions was demonstrated by use of the graphite boat with no lid fitted, which gave rise to a far poorer degree of ZrC formation as evidenced by XRD (data not shown).

3.4. *Porosimetry and surface area measurements*

Surface area data are presented in Table 3. After heating to 1350 °C under reducing and carburising conditions, the materials produced by alkoxide co-precipitation not only had poor compressive strength but also low surface areas. In contrast, the materials from the halide co-precipitation and alkoxide infiltration routes were moderately robust and for the most part also had high surface areas. Several of the high temperature treated alkoxide infiltration materials showed high surface areas that it is surmised must be due at least in part to the additional surface area added by the zirconia film. However, the much lower surface area of the PAN beads heated in the same way probably reflects shrinkage of the PAN resulting in loss of accessibility to some of the pore system. In the former case, the ZrO_2 films may assist in maintaining accessibility by providing a rigid wall preventing complete closure of the pore system. However, if this ZrO_2 film exceeds a certain thickness (ZrAI-4), it can begin to occupy significant pore space reducing the total surface area considerably.

The halide co-precipitation materials showed an inverse relationship with respect to surface area before and after high temperature treatment. $ZrCl_4$ should hydrolyse on contact with water to form aqueous $ZrOCl_2$, which should immediately precipitate as hydrous ZrO_2 in the alkaline bath [26]. For the materials pretreated at 240 ° C the surface area increases with Zr content while for materials converted at 1350 °C, the surface area decreases with Zr content. For the ZrHC-x materials the sample purity also increased

Table 2
Rietveld refinement results for the ZrHC-x series of samples. Errors estimates in the cell parameters are given in parentheses and reflect the uncertainty in the last significant figure.

Sample	Phase	%	a (Å)	b (Å)	c (Å)	b (deg)	Vol (Å^3)
ZrHC-1	ZrC	90.1	4.67411 (7)	4.67411 (7)	4.67411 (7)	**e**	102.1185
	$tZrO_2$	5.5	3.64 (1)	3.64 (1)	3.64 (1)	**e**	68.51
	$mZrO_2$	4.4	4.70 (2)	5.74 (2)	4.69 (1)	97.2882	125.62
ZrHC-2	ZrC	95.8	4.67267 (3)	4.67267 (3)	4.67267 (3)	**e**	102.0232
	$tZrO_2$	4.2	3.6 (2)	3.6 (2)	5.2 (8)	**e**	68.14
ZrHC-3	ZrC	99	4.6791 (1)	4.6791 (1)	4.6791 (1)	**e**	102.3408
	$tZrO_2$	1	3.62 (1)	3.62 (1)	5.19 (4)	**e**	67.91
ZrHC-4	ZrC	98.4	4.67358 (5)	4.67358 (5)	4.67358 (5)	**e**	102.0818
	$tZrO_2$	1.6	3.62 (9)	3.62 (9)	5.2 (3)	**e**	67.91

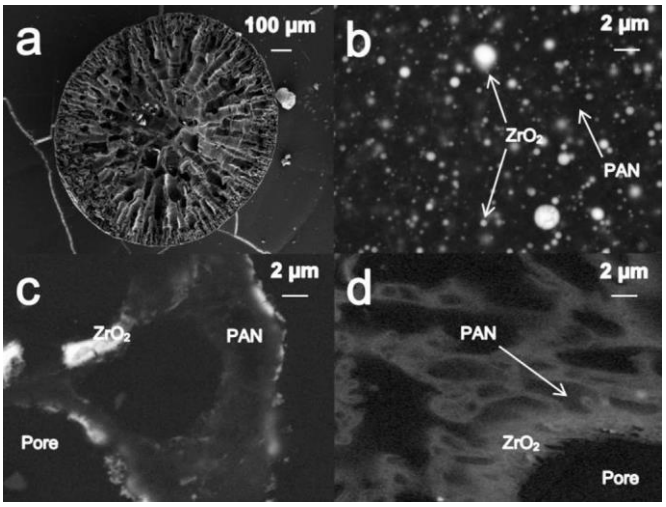

Fig. 4. SEM backscattered electron images: a) a representative example of the radial pore structure of PAN composite beads; microstructures of 240 °C stabilised b) ZrAC-1, c) ZrHC-1 and d) ZrAI-1, respectively, showing different mixing of PAN and zirconia.

with increasing Zr content. We hypothesized that the surface area that is measured depends on the ZrO_2 nanoparticle content of the materials generated at the two different temperatures. As more Zr is included in the precursor, more ZrO_2 nanoparticles are generated on co-precipitation. After pretreatment at 240 °C, the surface area depends on the concentration of these nanoparticles which is directly proportional to the Zr content. After carbothermal reduction at 1350 °C, the ZrO_2 nanoparticle content generally decreases as the initial Zr content increases and therefore the surface area also decreases.

Nitrogen adsorption isotherms as well as pore size distributions calculated using both the BJH (desorption branch) and the NLDFT method for large batches of the two materials having high surface areas, ZrAI-2 and ZrHC-1, are shown in Fig. 5. Both isotherms appear to be hybrids or combinations of type I, II and IV isotherms according to the IUPAC classification [27], respectively indicative of microporous, non-porous and mesoporous materials. In this context, type II (non-porous solid) is interpreted to mean that macropores, not normally measurable by the nitrogen adsorption technique, are present. Of the two isotherms the hysteresis appears to be more pronounced for the ZrAC-1 material. According to cur- rent wisdom this type of hysteresis with a sudden drop off in the amount of nitrogen adsorbed is typical of cavitation effects resulting from ink-bottle pores. The hysteresis shapes (type B by the classification system of de Boer [28]) indicate irregular shaped

Table 3
BET surface areas of heat treated materials.

Sample	S.A.$_{BET}$ (m^2/g) 240 °C, air	S.A.$_{BET}$ (m^2/g) 1350 °C, 3.5% H_2–Ar
PAN	6.1	9.4
ZrAC-1	4.8	72
ZrAC-2	5.7	6.4
ZrAC-3	6.8	2.3
ZrAC-4	30	2.2
ZrHC-1	29	73
ZrHC-2	33	50
ZrHC-3	39	32
ZrHC-4	42	27
ZrAI-1	12	44
ZrAI-2	11	72
ZrAI-3	7.9	73
ZrAI-4	38	6.1

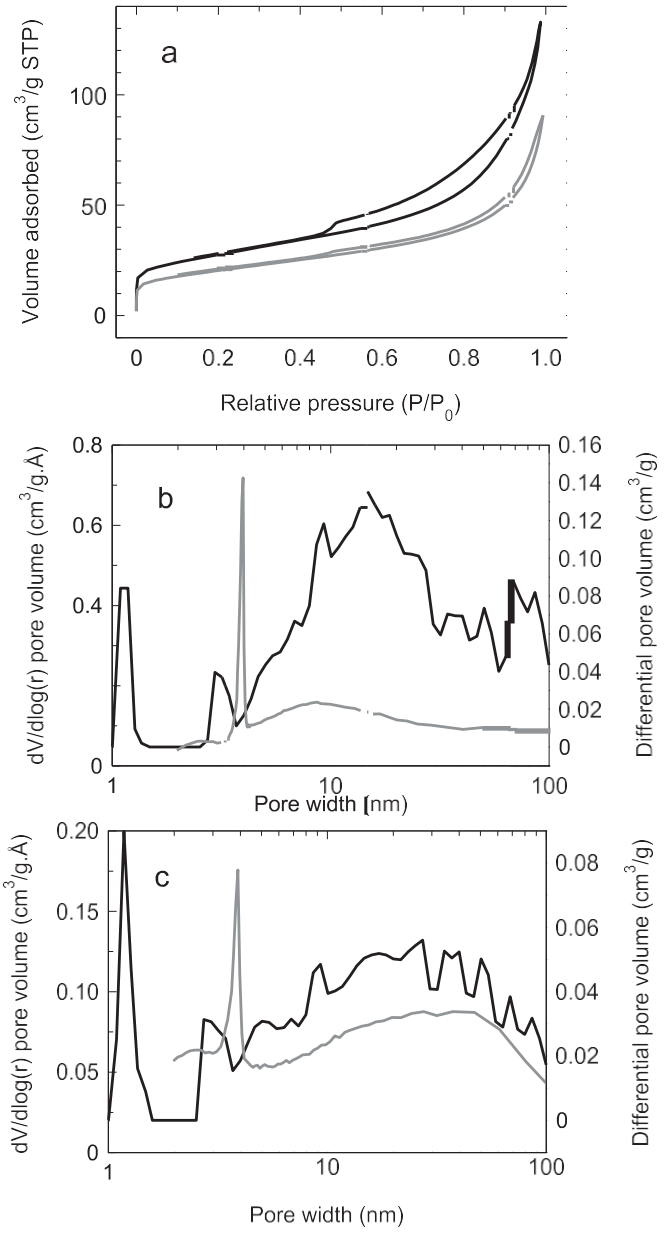

Fig. 5. a) Nitrogen adsorption–desorption isotherms. Key: grey, ZrAI-2; black, ZrHC-1. b) Pore size distribution for ZrAI-2. c) Pore size distribution for ZrHC-1. Key for both b) and c): grey, BJH; black, NLDFT. BJH is plotted against left axis and NLDFT is plotted against right axis.

pores or a mixture of different pore shapes. In the case of both materials analysis of the pore size distributions (PSD) using the traditional BJH approach (Fig. 6b and c) yields a sharp peak at 3.9 nm and a broad distribution of pores greater than about 6 nm. Since the sharp feature is probably an artefact we also analysed the isotherms using NLDFT which models only the adsorption branch. A slit pore model was used in the analyses since generally it gave a better fit between the experimental and theoretical isotherms. In fact the PSD calculated using NLDFT show some similarities with those calculated using the BJH methodology. For instance the broad pore distribution of pores in the range 6–100 nm appears to be reproduced. Moreover, smaller peaks are observed in both cases around 1.2 and 3.0 nm. Although these sharper peaks are broader than the artefact determined using BJH they are nonetheless quite well defined. The pore structure of the both the ZrHC-x and ZrAI-x

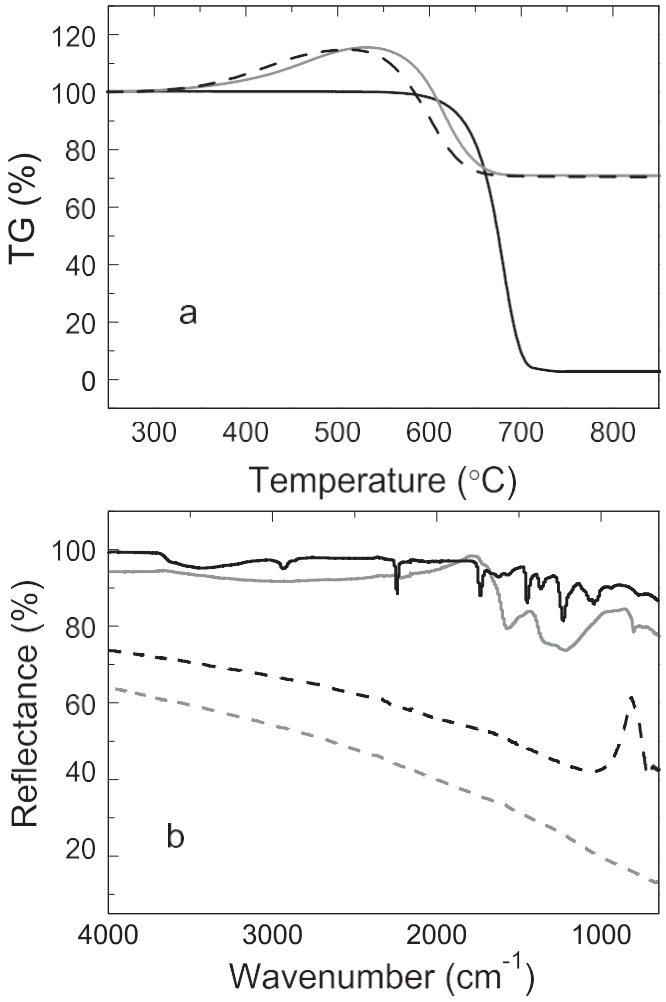

Fig. 6. a) Thermogravimetric behaviour in air of 1350 °C heat-treated materials. Key: black, PAN-1350; grey, ZrHC-1; dashed black, ZrAI-2. b) FT-IR spectra demonstrating evolution of bonding during heat treatments. Key: black solid, PAN powder; grey solid, PAN-240; black dashes, ZrAI-5; grey dashes, PAN-1350.

materials therefore appears to be hierarchical with distinct pore distributions centred at around 1, 3 and 20**e**30 nm.

Taken together with the microscopy data presented earlier, which visually demonstrated the presence of macropores, clear evidence of a hierarchy of porosity is apparent in both systems. The practical consequence of this hierarchical porosity is that the ma- terials would be expected to be well-suited for use in a flow- through application, such as in a column, wherein efficient intra- particle diffusion is required. Moreover, the radial macropore structure remarked upon earlier may improve this diffusion pro- cess. While examples in the literature abound for hierarchically porous carbons, to the best of our knowledge, there is no precedent for hierarchically porous zirconium carbides. A similar isotherm shape, however, was recently reported by Drisko and co-workers for carbonised PAN-zirconium titanium oxide composite beads [29].

3.5. Thermogravimetric analysis (TGA) and FT-IR

TGA curves in air are given in Fig. 6a. PAN-1350 beads that were previously heated to 1350 °C under reducing and carburising conditions, rapidly and continuously lost weight above 600 °C, leaving a residue of only a few wt%. In contrast, the two composites heat treated in the same way gained approximately 15 wt% when heated in air starting from 300 °C. A previous study found that ZrC does not oxidise appreciably in atmospheric concentrations of oxygen until nearly 700 °C [30]. If this is indeed the case, the results presented here could be explained by surface re-oxidation of ZrO_2 phases in the two samples which may have been left sub-stoichimetric (i.e. ZrO_{2x}) by the high temperature reducing treatment. This explanation is consistent with the Rietveld analysis of the XRD data indicating the presence of zirconia phases in these same bead materials. Alternatively, ZrC may have oxidised, in which case factors such as ZrC particle size and/or Zr-carbon stoichiometry may play a role in the oxidation temperature of ZrC, not considered by this previous study.

FT-IR spectroscopy (Fig. 6b) of 240 °C-stabilised PAN beads when compared with as-received PAN powder, showed a change in position of absorption bands corresponding to cyclisation of the nitrile group to form a conjugated ring structure [31]. Upon further heating of the PAN beads to 1350 °C under carburising and reducing conditions (PAN-1350), nearly all discernible bands disappeared from the spectrum. An example of one of the composites also shows a single band at low wavenumbers. When various amorphous and monoclinic zirconias were analysed (data not shown), only the monoclinic zirconias showed this band, therefore this is attributed to the presence of $mZrO_2$. The presence of this band in various composites was in agreement with the identified $mZrO_2$ phase in the XRD patterns for the same materials.

The reducing and carburising heating conditions markedly affected the surface chemistry of the materials. PAN is a N-rich polymer (*ca*. 26 wt%) which takes on up to 20 wt% of O when stabilised in air. The heteroaromatic N- and O-containing structure of air-stabilised PAN has been extensively investigated by other workers [32]. The disappearance of absorption bands in the FT-IR spectra for the PAN-derived carbon beads indicates that nearly all C**e**N and C**e**O bonding was lost, which amounts to removal of most N and O heteroatoms from the carbon structure. Apart from the presence of an absorption band in those samples containing $mZrO_2$ due to this phase, all other absorption bands were removed from the composites. Further confirmation came from C, H, N micro-analysis of PAN-1350 which returned C, H and N contents, respectively, of 98.9, 0.0 and 0.6 wt%. The balance (0.5 wt%) is presumed to be O.

3.6. Adsorption studies

Initial non-radioactive scoping studies using common elements were conducted to elucidate the fundamental adsorption proper- ties of the unfunctionalised bead materials. The selectivity of the materials as a function of solution pH for the materials ZrAI-2 and ZrHC-1 are presented in Fig. 7a and b. The pH dependence of the actinide U and fission product elements Cs, Sr and Mo were investigated. Notably, these materials did not show any affinity for Cs and only adsorbed Sr under alkaline conditions. The materials showed high affinity for U from pH 4.7 to pH 11.5 and Mo from approximately pH 1.9 to pH 3.4. Under these respective conditions, U mainly exists as hydrolysed uranyl dimeric and trimeric cationic species whereas Mo exists as the neutral monomeric species, H_2MoO_4 and anionic hydrolysis products $HMoO_4^-$ and MoO^{2-} [33].4 In the usable range for Mo, the materials showed negligible adsorption of Cs, Sr and U. These results foreshadow a possible means of loading MAs onto the beads. Provided that the anion exchange properties hold true, MAs might be adsorbed as the anionic complexes of ligands containing low neutron cross section elements, such as O, C and H, under moderately acidic conditions. The impediment posed by the mostly trivalent lanthanide isotopes, which are largely neutron poisons, and the great challenge in separating them from the trivalent MAs (Am and Cm) with whom

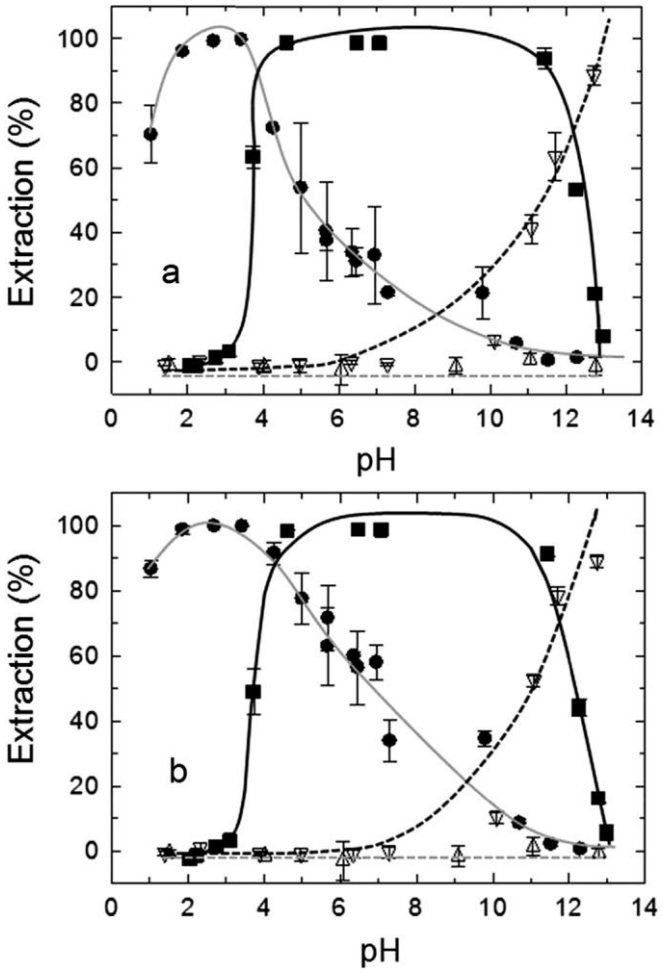

Fig. 7. a) pH dependence of metal adsorption onto ZrHC-1; b) pH dependence of metal adsorption onto ZrAI-2. (7) Sr; (▵) Cs; (—) U; (C) Mo. The lines are intended as a guide to the eye only.

they share very similar chemistries, is well known [34]. Consequently, whether the MAs can be selectively removed in the presence of the lanthanide group of fission products in waste streams using these bead materials would need to be addressed. If this situation proves intractable, then appropriate surface modification or a pre-separation prior to MA loading would be necessary. At the time of writing, we are working towards establishing a clearer picture of trivalent lanthanide/MA selectivity for these novel materials, which would form the subject of another contribution.

In order to assess the ability of the porous zirconium carbide spheres to sorb a target element and then recover it, the ZrHC-1 material was contacted with a nitric acid solution of Mo at pH of 3. According to the results of Fig. 7a, at this pH Mo sorbs quantitatively. Extraction of the Mo using NaOH solution with pH of 11 results in almost quantitative recovery of Mo as expected from Fig. 7a. This process of adsorption and desorption could be carried out repeatedly without appreciable loss of either adsorption or percentage recovery at least over four cycles (Table 4). Thus the present zirconium carbides show excellent recyclability although it may not be required for the particular application being considered.

4. Conclusions

Hierarchically porous granular materials based on PAN have been synthesised by three different methods, referred to as

Table 4
Results of adsorption–desorption cyclability. The pH of adsorption was 3.0 ± 0.2 and for desorption was 11.0 ± 0.2. The Mo concentration in solution was 0.025 mmol/L and the volume-to-mass ratio was 200 ml/g.

Cycle	Adsorption (%)	Desorption (%)
1	>99	86
2	>99	91
3	>99	96
4	>99	83

alkoxide co-precipitation (AC), alkoxide infiltration (AI) and halide co-precipitation (HC). The AI and HC methods produced relatively robust materials with generally high surface areas. In all cases, the high temperature reducing and carburising conditions yielded conversion of ZrO_2 to ZrC. Of the three methods, the two based on co-precipitation of the Zr precursors with PAN might a priori be expected to lead to more intimate contact between the C and Zr sources. However, Rietveld analysis suggests that the highest yields of ZrC were obtained for ZrHC-3 (99%) and ZrAI-3 (96.5%). The highest yield for the alkoxide co-precipitation series was obtained for the ZrAC-1 sample (88%). The data suggest that the yield of ZrC was dependent on both method and composition. The pH dependence of adsorption of U and fission product elements Cs, Sr and Mo was studied. It was found that the materials showed no affinity whatsoever for Cs and adsorbed Sr only at relatively high pH values. Mo and U in contrast, adsorbed selectively at different pH values in the low pH region. The idea was advanced of using the materials as reusable transmutation targets for the burn-up of long-lived radionuclides, especially MAs. In this regard, their hierarchical porosities facilitate their use in column or flow-through processing. Although the present results do offer hope for being able to use porous ZrC adsorbents that can be loaded and subjected to neutron irradiation and then unloaded in a cyclical fashion, much remains to be addressed. For instance, intense radiation fields and the generation of high energy fission fragments can result in structural changes to the host matrix in addition to changes to molecular speciation that can profoundly alter functionality and implementation.

Acknowledgements

The authors wish to express their appreciation to the ANSTO for supporting this research and the following individuals for their contributions: Mr Joel Davis of ANSTO for SEM analysis; Mr Brett Rowling and Mr Henri Wong of ANSTO for ICP-MS analysis of recyclability tests; Mr Kevin Thorogood of ANSTO for drafting the design of the carbon boat; Dr Weimin Zhang of University of Wollongong, IPRI, for TGA; Mr Tim Palmer of ANSTO for guidance in optical microscopy sample preparation; Dr Ken Short and Mr John Bowdler of ANSTO for their hard work in maintaining and repairing our tube furnace. The droplet generator used in synthesis was built by Dr Erden Sizgek, formerly of ANSTO. C, H, N microanalysis was conducted on a pay per sample basis at the Microanalytical Centre, Research School of Chemistry, Australian National University. The authors also acknowledge the Australian National Fabrication Facility (ANFF) for the provision of service and equipment access.

Appendix A. Supplementary data

References

[1] L.L. Snead, Y. Katoh, S. Kondo, J. Nucl. Mater. 399 (2010) 200–207.

[2] K. Minato, et al., J. Nucl. Mater. 279 (2000) 181e188.
[3] K. Minato, et al., J. Nucl. Mater. 252 (1e2) (1998) 13e21.
[4] D. Gosset, et al., J. Nucl. Mater. 373 (2008) 123e129.
[5] S. Pillon, Actinide-bearing Fuels and Transmutation Targets, Elsevier B.V, 2012.
[6] T. Todd, Chemistry of the Nuclear Fuel Cycle e Applied Aspects, American Chemical Society, 2012.
[7] S. Bourg, et al., ACSEPT e Status in Advanced Separation Process Developments in Europe, Societe Francaise d'Energie Nucleaire, 2012.
[8] F.W. Clinard, et al., J. Nucl. Mater. 1e3 (1984) 1386e1392.
[9] F.A. Garner, et al., J. Nucl. Mater. 212e215 (1994) 1087e1090.
[10] R.J.M. Konings, et al., J. Nucl. Mater. 254 (1998) 135e142.
[11] N. Chauvin, et al., J. Nucl. Mater. 274 (1999) 91e97.
[12] T. Yano, et al., J. Nucl. Mater. 283e287 (2000) 947e951.
[13] D. Warin, et al., in: Proceedings of the International Conference Global 2001 on Back-end of the Fuel Cycle: from Research to Solutions. 2001. Paris, France, Sept 9e13, 2001.
[14] S. Pillon, et al., in: Proceedings of the International Conference Global 2001 on Back-end of the Fuel Cycle: from Research to Solutions. Paris, France, Sept 9e13, 2001.
[15] J. Noirot, et al., J. Nucl. Mater. 320 (2003) 117e125.
[16] E.A.C. Neeft, et al., J. Nucl. Mater. 320 (2003) 106e116.
[17] J.M. Bonnerot, et al., in: Proceedings of the International Conference Global 2007 on Advanced Nuclear Fuel, Cycles and Systems. 2007. Boise, ID, Sept 9e13, 2007.
[18] D. Staicu, et al., in: Proceedings of the International Conference Global 2009 on the Nuclear Fuel Cycle: Sustainable Options & Industrial Perspectives 2009: Paris, France, Sept 6e11, 2009.
[19] K. Richter, A. Fernandez, J. Somers, J. Nucl. Mater. 249 (1997) 121e127.
[20] J. Somers, A. Fernandez, Prog. Nucl. Energy 48 (2006) 259e267.
[21] A. Fernandez, et al., J. Am. Ceram. Soc. 85 (3) (2002) 694e696.
[22] G. Vasudevamurthy, et al., J. Nucl. Mater. 374 (1e2) (2008) 241e247.
[23] M.D. Sacks, et al., J. Mater. Sci. 39 (2004) 6057e6066.
[24] A.J. Clarke, J.E. Bailey, Nature (London, United Kingdom) 243 (5403) (1973) 146e150.
[25] Y. Katoh, et al., J. Nucl. Mater. 441 (2013) 718e742.
[26] A. Clearfield, Rev. Pure Appl. Chem. 14 (1964) 91e108.
[27] K.S.W. Sing, et al., Pure Appl. Chem. 57 (1985) 603.
[28] J.H. de Boer, in: The Structure and Properties of Porous Materials, Butterworth, London, 1958, p. 68.
[29] G.L. Drisko, et al., ACS Appl. Mater. Interfaces 5 (2013) 5009e5014.
[30] T.F. Viotovich, E.A. Pugach, Poroshkovaya Metall. (Kiev) 131 (1973).
[31] W.J. Burlant, J.L. Parsons, J. Polym. Sci. 22 (1956) 249e256.
[32] M.S.A. Rahaman, A.F. Ismail, A. Mustafa, Polym. Degrad. Stab. 92 (8) (2007) 1421e1432.
[33] Baes, C.F. and R.E. Mesmer, The Hydrolysis of Cations. Malabar: Robert E. Krieger Publishing Company, Inc.
[34] G.R. Choppin, J. Alloys Compd. 223 (2) (1995) 174e179.